1 **Assessment of ICESat-2 sea ice surface classification with Sentinel-2 imagery:**

2 **implications for freeboard and new estimates of lead and floe geometry**

3 A. A. Petty[1,2], M. Bagnardi[2,3], N. Kurtz[1], R. Tilling[1,2], S. Fons[2,4], T. Armitage, C. Horvat[5], R.

4 Kwok[6]

5 [1] Earth System Interdisciplinary Center, University of Maryland, College Park, MD, USA

6 [2] NASA Goddard Space Flight Center, Greenbelt, MD, USA

7 [3] ADNET Systems, Inc., Bethesda, MD, USA

8 [4] Department of Atmospheric and Oceanic Sciences, University of Maryland, College Park, MD,
9 USA

10 [5] Brown University, Providence, RI, USA.

11 [6] University of Washington, Seattle, WA, USA.

12

13 Corresponding author: Alek A. Petty (alek.a.petty@nasa.gov)

14 **Key points**

15 • Specular leads identified by ICESat-2 show strong agreement with leads observed in
16 coincident Sentinel-2 imagery.

17 • The coincident images provide further evidence of the misclassification of dark leads due
18 to clouds, which are no longer used to derive freeboard in ICESat-2 data.

19 • We apply two metrics for estimating lead fraction and chord length across the entire
20 Arctic and Southern Ocean.

21 **Abstract**

22 NASA's Ice, Cloud, and Land Elevation Satellite-2 (ICESat-2) mission launched in September

23 2018 and is now providing high-resolution surface elevation profiling across the entire globe,

24 including the sea ice cover of the Arctic and Southern Oceans. For sea ice applications,

25 successfully discriminating returns between sea ice and open water is key for accurately

26 determining freeboard (the extension of sea ice above local sea level) and new information

27 regarding the geometry of sea ice floes and leads. We take advantage of near-coincident optical

28 imagery obtained from the European Space Agency (ESA) Sentinel-2 (S-2) satellite over the

29 Western Weddell Sea of the Southern Ocean in March 2019 and the Lincoln Sea of the Arctic

30 Ocean in May 2019 to evaluate the surface classification scheme in the ICESat-2 ATL07 and

31 ATL10 sea ice products. We find a high level of agreement between the ATL07 (specular) lead

32 classification and visible leads in the S-2 imagery in these two coincident images across all six

33 ICESat-2 beams, increasing our confidence in the freeboard products and deriving new estimates

34 of the sea ice state. The S-2 overlays provide additional, albeit limited, evidence of the

35 misclassification of dark leads due to clouds. Dark leads are no longer used to derive sea surface

36 and thus freeboard as of the third release (r003) of the ICESat-2 sea ice products. We show

37 estimates of lead fraction and more preliminary estimates of chord length (a proxy for floe size)

38 using two metrics for classifying sea surface (lead) segments across both the Arctic and Southern

39 Ocean for the first winter season of data collection.

40   1. Introduction

41 NASA's Ice, Cloud, and Land Elevation Satellite-2 (ICESat-2) is a new satellite mission

42 providing unprecedented (high resolution and accuracy) profiling of the Earth's surface,

43 especially over the high-latitude polar regions. ICESat-2 was launched successfully from

44 Vandenberg Air Force Base on September 15th, 2018 and started acquiring science quality data

45 on October 14th, 2018. A description of the ICESat-2 mission design and objectives can be

46 found in Markus et al., (2017) and Neumann et al., (2019).

47   ICESat-2 consists of a bespoke photon-counting Advanced Topographic Laser Altimeter

48 System (ATLAS) - a low pulse-energy laser split into a novel six-beam configuration of three

49 beam pairs (a strong and a weak beam). At the nominal orbital altitude, ATLAS generates

50 individual laser footprints of ~11 m (in diameter) on the Earth's surface (Magruder et al., 2020).

51 The high pulse repetition rate of 10 kHz means laser pulses are separated by only 70 cm along-

52 track; a much higher resolution and sampling than NASA's previous laser altimetry mission

53 ICESat (Zwally et al., 2002). ICESat-2 samples year-round and has only experienced minimal

54 downtime since launch.

55   Various data products are now being generated routinely from ICESat-2 which are

56 publicly disseminated through the National Snow and Ice Data Center (NSIDC,

57 https://nsidc.org/data/icesat-2). The primary science data product from ICESat-2 is the Level 2A

58 ATL03 geolocated photon heights (Neumann et al., 2019) from which most of the higher-level

59 science products are derived. For sea ice users, the primary products of interest are the Level 3A

60 along-track sea ice height and type (ATL07, https://nsidc.org/data/ATL07) and freeboard

61 (ATL10, https://nsidc.org/data/ATL10) products (Kwok et al., 2020a). The first winter-season of

62 Arctic sea ice heights and freeboards (October 2018 to March 2019) were presented in Kwok, et

63 al., (2019a). Sea ice thickness has been estimated from these freeboards using external snow

64 loading estimates from the NASA Eulerian Snow on Sea Ice Model (NESOSIM) and modified

65 versions of the Warren climatology (Petty et al., 2020) and through the combination of total (ice

66 plus snow) freeboard from ICESat-2 with estimates of ice freeboard from the CryoSat-2 radar

67 altimeter to derive snow depth and freeboard concurrently (Kwok et al., 2020b). The surface

68 heights and freeboards were assessed against coincident airborne elevation data collected by

69 NASA's Operation IceBridge (Kwok et al., 2019b). The along-track heights generated from the

70 Airborne Topographic Mapper (ATM, Studinger, 2014) flown on OIB showed strong agreement

71 with ATL07-derived heights, while the derived freeboard from ATM showed only small (0-4

72 cm) differences with ATL10 freeboards, depending on the method used to derive and compare

73 freeboard. Coincident imagery obtained during the OIB surveys by the Continuous Airborne

74 Mapping By Optical Translator (CAMBOT) alluded to erroneous classification of 'dark leads' in

75 the presence of clouds (Kwok et al., 2020c). A dark lead classification is associated with a dark

76 surface and relatively low photon rates unlike the high photon rates associated with specular

77 leads (described more in Section 2.1). The dark lead segment classification is still included in the

78 latest (r003) ATL07 sea ice height and surface classification product release, but these have now

79 been excluded from the derivation of freeboard in the latest (r003) ATL10 product release (the

80 ATL07 and ATL10 products are described more in the following section). This change remains

81 in-place for the upcoming r004 data release. The Kwok et al., (2020c) study highlighted the

82 significant utility of coincident high-resolution imagery for better understanding the performance

83 of the ICESat-2 sea ice surface classification algorithm. The assessment, however, was hindered

84 by the high consolidation of the ice pack in the region profiled during the spring 2019 OIB

85 campaign, limiting the number of leads/open water segments and the quality of the freeboard

86 estimates due to the lack of reliable sea surface tie-points.

87   The main objective of this study is to further assess the performance of the surface

88 classification scheme in ATL07 for discriminating between sea ice and open water. We take

89   advantage of near-coincident optical imagery from the Sentinel-2 satellite mission to assess this

90   specific aspect of the ATL07 algorithm performance. Successfully discriminating returns

91   between sea ice and open water has benefits beyond deriving freeboard. Additional metrics for

92   understanding the sea ice state include concentration, lead fraction (or density) and floe size. In

93   the marginal seas, where waves can break up and fracture the ice (Horvat et al., 2020 and

94   references therin), ice floes are thought to be smaller and less concentrated/consolidated (a

95   higher lead fraction) than within the pack ice. The geometry of floes and leads is an important

96   control on the strength of sea ice and its thermodynamic response to forcing (Feltham, 2005;

97   Horvat et al., 2016), particularly in marginal, coastal, and seasonally-ice-covered seas. The floe

98   size distribution (Rothrock & Thorndike, 1984) is increasingly being introduced into sea ice

99   components of climate models (Bateson et al., 2020; Roach et al., 2018) , but only limited basin-

100   scale observational constraints exist to-date, e.g. estimates derived from ESA's CryoSat-2 radar

101   altimeter for the Arctic Ocean only (Horvat et al., 2019). ICESat-2 offers the exciting potential to

102   provide new observational estimates of the floe size distribution, benefiting from the small

103   footprint, high precision and along-track sampling rate across the multiple beams. Satellite tracks

104   (e.g. those from ICESat-2) profile ice floes across random/unknown cross sections of the floe.

105   The along-track cross section of a floe measured by satellite is commonly referred to as a chord

106   length. A collection of floe chord lengths can provide statistics of floe geometry, e.g. moments of

107   the floe size distribution and the open water fraction, under certain assumptions about the

108   underlying floe geometry (Horvat et al., 2019).

109   The coincident S-2 scenes provide the ideal means for assessing new lead fraction and

110   chord length estimates from ICESat-2 data, complementing the freeboard/thickness estimates

111   already being generated. We choose to discuss lead fraction instead of sea ice concentration as

112   concentration/extent was discussed in Horvat et al., (2020) and an assessment/comparison with

113   the commonly used passive microwave-derived concentrations (taking into account the

114   significant sampling differences) is beyond the scope of this study.

115   ## 2. Data

116   ### 2.1 ATL07 sea ice heights and surface classification

117   We primarily use data from the ICESat-2 ATL07 sea ice height and type product. A full

118   description of the ATL07 product can be found in the ATL07/ATL10 Algorithm Theoretical

119   Basis Document (ATBD, Kwok et al., 2020a) and the recent changes to this algorithm for

120   Release 003 (r003) are discussed more in Kwok et al., (2020c), so here we provide only a basic

121   overview of the methodology relevant to the results/discussion presented in this study.

122   ATL07 is generated by aggregating 150 photons from the ATL03 geolocated photon

123   product (Neumann et al., 2019) independently along each of the six beams. The beams are

124   arranged in 'strong' and 'weak' beam pairs with each beam pair separated by ~3.3 kilometers in

125   the across-track direction and the strong/weak beams separated by ~90 m across-track and ~2.5

126   km along-track. A surface finding routine (ATL07/10 ATBD r003, section 4.2) first windows the

127   photon heights around an expected sea surface then extracts a best-guess Gaussian height

128   distribution (convolved with the expected system response) to the photon height histogram to

129   determine 1) a single segment height, 2) an associated quality flag based on the goodness of fit

130   and 3) associated metrics including photon rate. The heights are expressed relative to the WGS84

131   ellipsoid with the mean sea surface (MSS) and various time-variable geophysical corrections

132   removed: ocean tides, solid earth tides, ocean loading, solid earth pole tides, inverted barometer.

133   Surface-classified height segments are produced for each of the six beams (three strong and weak

134   pairs) independently. The photon rates of the strong beam are roughly 4 times higher than those

135   of the weak beam, which results in mean segment lengths of ~15 m for the strong beam and ~60

136   m for the weak beam (Kwok et al., 2019a). Adding the individual laser footprint size of ~11 m to

137   the segment length provides an estimate of the spatial resolution of the segments (i.e. a mean of

138   ~26 m x 11 m for the strong beam and 71 m x 11 m for the weak beam).

139   An empirically based decision-tree algorithm is used to discriminate the returns between

140   sea ice and open water (Kwok et al., 2016). The empirical thresholds were determined

141   principally by 1) data collected in campaigns prior to the launch of ICESat-2 by the Multiple

142   Altimeter Beam Experimental Lidar (MABEL) - a test-bed instrument for ICESat-2 (McGill et

143   al., 2013); and 2) post-launch evaluation of the ATLAS performance. The three inputs to this

144   decision tree (and the physical justifications) are as follows:

145   1. Photon rate (photon returns per laser pulse, the apparent reflectivity of the surface).
146   Low photon rates are associated with water or very thin ice in open leads, which are
147   generally darker than sea ice. However, specular and quasi-specular returns have
148   been observed from smooth open water/thin ice surfaces in both ICESat and MABEL.
149   2. Width of the Gaussian fit to the photon height distribution (the small-scale surface
150   roughness). Used to partition the surface types into smooth/rough categories.
151   3. Background rate (deviations compared to the photon rate indicate shadows, specular
152   reflections and/or atmospheric contamination).

153   The result of the decision tree determines the radiometric surface type which includes the
154   following classifications (denoted by the *height_segment_type* flag): cloud (0), snow covered,
155   gray or rough ice (1), specular leads (2-5), smooth dark leads (6-7) and rough dark leads (8-9).
156   This is considered the winter-time decision tree. As discussed in the introduction, in the latest
157   ATL10 data release (r003), dark lead segments (*height_segment_type* = 6 to 9) have been
158   dropped from the derivation of the local reference sea surface height (as detailed below) due to
159   possible issues with cloud attenuation, so now only specular leads (*height_segment_type* = 2 to
160   5) are used for deriving the reference sea surface height and freeboard (Kwok et al., 2020c).

161   Due to the expected uncertainty in this radiometric surface classification approach (Kwok
162   et al., 2016), a further filtering is applied based on the local height distribution:

163   4. Local height filter, based on the distribution of local (10 km) smooth height segments
164   (h_{sm}) – segments with a Gaussian width < 0.13 m. Specifically the lead segment
165   height must be between the minimum of the smooth heights (h_{sm_min}) and the
166   maximum of either the 2nd percentile of the smooth heights or h_{sm_min} + 2 σ where σ =
167   2-3 cm, the expected uncertainty in surface height over smooth surfaces.

168   The result of the radiometric decision tree and local height filter sets the sea surface
169   height flag (*ssh_flag, 0 = sea ice, 1 = sea surface*). Sea surface segments are considered
170   candidate lead segments for deriving the reference sea surface height and thus freeboard in
171   ATL10. Note that the summertime (non-winter) decision tree simply extends the classification of
172   ice, specular leads and dark leads as potential melt ponds (not a feature of this analysis).

173   Freeboards are calculated in ATL10 in 10 km along-track sections based on a reference
174   sea surface derived from the available lead/sea surface segment heights (ATL07/10 ATBD r003,

175   section 5.1). Briefly, consecutive sea surface segments are grouped together into individual

176   'leads' (to reduce noise in the individual sea surface estimates) before a single reference sea

177   surface estimate is produced for consecutive 10 km along-track sections that include at least one

178   sea surface segment, for each beam independently. A basic interpolation/end-filling procedure is

179   used to extend the reference sea surface estimates into regions where a sea surface segment does

180   not exist. A filtering is also applied to ensure that the 10 km sections are at least 25 km away

181   from the coast and have a concentration (from passive microwave data) > 50 % - i.e. within the

182   pack ice and away from regions thought to be more affected by waves. The 10 km reference sea

183   surface heights must also lie within a set height window relative to the MSS (+/- 0.5 m for the

184   Arctic and +/- 1 m for the Southern Ocean) and differences between consecutive sea surface

185   heights must be relatively small (see the ATL07/10 ATBD r003, section 5 for more details).

186   After the filtering, *candidate lead* segments (i.e. segments with *ssh_flag* = 1) used to generate a

187   reference sea surface that also pass the above filters are set as *lead* segments (*ssh_flag* = 2) to

188   make clear they have indeed been used to derive the reference sea surface height and thus

189   freeboard in ATL10. Freeboard segments are then derived by differencing the sea ice segment

190   heights from the local 10 km reference sea surface height. Negative freeboards are set to zero.

191   More detail about the methodology is given in Kwok et al., (2020a) and Kwok et al., (2020c).

192   **2.2 Sentinel-2 imagery**

193   Sentinel-2 is a constellation of two twin satellites, Sentinel-2A (S-2A) and Sentinel-2B

194   (S-2B), operated by the European Space Agency (ESA) and launched in June 2015 and March

195   2017, respectively. The satellites host the MultiSpectral Instrument (MSI), which provides 13

196   reflective-wavelength bands in the wavelength region between 443 nm and 2202 nm (visible,

197   near-infrared, short-wave infrared). Depending on the band, spatial resolution varies between 10,

198   20, and 60 m, with the images covering an area of ~ 110 km x 110 km. For a given area, the shift

199   by 180 degrees between the two sun-synchronous polar orbits and a 290 km wide swath

200   guarantee a revisit time of 5 days at the equator, which improves to one image per day at higher

201   latitudes due to overlapping swaths with different viewing angles. Systematic global coverage of

202   land surfaces and coastal waters (up to 20 km from the coast) is available between 84 °N and 56

203   °S. Additional imagery is collected near and over coastal regions of Antarctica, Baffin Bay and

204   the North Atlantic (https://sentinel.esa.int/web/sentinel/user-guides/sentinel-2-msi/revisit-

205   coverage).

206   We searched for coincident S-2 and ICESat-2 data over sea-ice covered portions of the

207   Arctic and Southern oceans. Our search algorithm matched the footprint of all S-2 images with a

208   nominal cloud coverage of less than 10% acquired during fall, winter, and spring months (fall

209   2018 to spring 2019) within the search regions (Arctic: Sep-May / Antarctic: Mar-Nov) with the

210   ICESat-2 reference ground track (RGT) times and locations (data from https://icesat-

211   2.gsfc.nasa.gov/science/specs). No images for winter months (e.g. December/January in the

212   Northern Hemisphere) are available due to the lack of sun illumination. We searched for

213   overlapping data pairs with an acquisition time difference of less than 2 hours to mitigate for ice

214   drift, resulting in 14 candidate S-2 images. This imagery subset was then checked for image

215   quality, presence/absence of sea ice, actual cloud cover, and for the extent of the overlap with

216   ICESat-2 data. Two optimal coincident images were found, 1) over the Lincoln Sea of the Arctic

217   Ocean in May 2019 (i.e. the end of winter, time difference of 94 minutes) and 2) over the

218   Western Weddell Sea of the Southern Ocean in March 2019 (i.e. the start of the austral winter,

219   time difference of only 7 minutes)*,* as shown in Figure 1. This Arctic Ocean scene occurs late in

220   the winter/spring season, after typical dates of melt onset in the Arctic. However, the location is

221   in the coldest/thickest ice of the Arctic and no surface melt is visible in the imagery. Visual

222   inspection of these scenes showed clear coincidence between the imagery and the ICESat-2 data

223   with no obvious issues of drift misalignment (no correction was applied). Half of the Southern

224   Ocean image is contaminated by clouds, as is clearly visible in Figure 1. We thus split these into

225   ~50 km along-track 'coincident profiles' for visualization purposes (two Arctic profiles and one

226   Southern Ocean profile). 50 km was also a good balance between data coverage and ease of

227   interpretation/visualization.

228   Note that manual drift alignment/correction was attempted for some of the other

229   candidate images but the lack of notable features (e.g., leads and ridges) hindered our efforts.

230   Manual drift correction was successfully applied in generating coincident summer S-2/ICESat-2

231   scenes, as shown in Tilling et al., (2020).

232   **3. Methods**

233   **3.1 Classification evaluation**

234   To compare the IS-2 ATL07/10 data with the S-2 imagery we use a simple nearest

235   neighbor interpolation scheme (the nearest geocoded pixel of the imagery to the given ATL07/10

236   beam segment) to produce a coincident profile of S-2 surface reflectance. In particular, we use

237   the red band, which is available at the highest 10 m spatial resolution and convert the Digital

238   Number (DN) provided in the Level-2A data products to surface reflectance by dividing by the

239   quantification value (DN/10,000). We compare these profiles qualitatively as the lack of perfect

240   time coincidence with the imagery, together with the possible impact of ice drift and the

241   contrasting resolutions of the data, make it challenging to carry out a more robust quantitative

242   assessment.

243   **3.2 Lead fraction**

244   To estimate lead fraction, we take the segment-length-weighted ratio of sea surface

245   segments to the total length of valid segments in 10 km along-track sections across the combined

246   three strong beams (we combine data from the 3 beams before sectioning the data). Note that the

247   IS-2 measurements include three beam pairs spread over ~6.6 km across-track, so for this to be

248   treated as a two-dimensional lead fraction estimate one needs to assume that the underlying ice is

249   isotropic and homogenous over this 10 km x 6.6 km window, something we plan to test more in

250   future work. The along-track lead fraction is calculated as

251
$$L_f = \frac{\sum_{N_{sl}} l_s^i}{\sum_{N_{all}} l_s^i}, \quad (1)$$

252   where l_s is the segment length, N_{all} is the total number of ice and lead segments in the given

253   section (10 km along-track in this study), N_{sl} is the total number of lead segments (specular only

254   in r003) and i is the height segment index.

255   The ATL07/10 sea surface classification approach is designed to be strict – i.e. possible

256   leads are potentially thrown away by the height percentile filter (step 4 in Section 2.1) to reduce

257   the likelihood of ice segments being erroneously used to derive a reference sea surface. This

258   approach makes sense when one considers the high sensitivity of the freeboard estimate to errors

259   in the reference sea surface height calculation. However, for ice floe/lead geometry analyses,

260   such a strict filter could result in an underestimate of lead fraction (and an overestimate of chord

261   length, discussed in the following section). We therefore adopt two approaches for deriving lead

262   fraction: i) L_f^{v1} where we use the ATL07 sea surface flag for candidate leads (*ssh_flag = 1*) and

263   ii) L_f^{v2} where we use the ATL07 specular lead classification (2 ≤ *height_segment_type* ≥ 5)

264   together with a less strict 10 km local height percentile filter (20% instead of 2%, see step 4 in

265   Section 2.1) to determine the sea surface segments. In summary L_f^{v1} is derived using the

266   *ssh_flag* from the product, whereas L_f^{v2} is derived using a higher 20% local height filter. This is

267   a relatively crude way of exploring the sensitivity of these lead estimates to the underlying

268   classification algorithm which we will aim to expand on in future work.

3.3 Chord length

270   To calculate chord length, we devised a simple algorithm that splits the along-track

271   segment data into floe (or chord) groups based on the sea surface classification flag. The sea

272   surface segments are discarded. Similar to lead fraction, we use two approaches here; C_l^{v1}

273   utilizes the sea surface flag (*ssh_flag*) and C_l^{v2} uses the sea surface classification derived in this

274   study using the 20% local height filter. In both cases a 'floe' group needs to include at least 3

275   height segments and have a maximum spacing between consecutive segments less than 300 m.

276   300 m is the upper end of the tail of the distribution of segment lengths for the strong beams

277   (Kwok et al., 2020a) meaning a gap between segments greater than this value is very likely to be

278   driven by the presence of anomalously high segment lengths (which are generally more

279   uncertain) or a data gap. Data gaps between segments are caused primarily by atmospheric

280   scattering (e.g. by clouds), which could result in erroneously high chord lengths, especially as

281   clouds can form preferentially over leads (although this is still being debated, e.g. Li et al.,

282   2020). We also discard any floe groups that are smaller than 60 m, which we take to be the

283   minimum resolved chord length due to considerations of footprint size and segment length, and

284   groups that are longer than 50 km. We add 11 m, the approximate photon footprint resolution, to

285   all groups to finally derive estimates of chord length. We run this analysis for each of the three

286   strong beams independently.

287   Note that we do not provide estimates of lead length in this study as estimates were provided

288   in Kwok et al., (2019a) and this is thought to depend more on the resolution of the ATL07 data,

289   so investigations focused on the underlying ATL07 algorithm may be needed to produce more

290   reliable lead length estimates in future work.

291   For both the lead fraction and chord length estimates, we bin the along-track data to a 25 km

292   x 25 km polar stereographic grid (EPSG:3411 for the Arctic and EPSG:3412 for the Southern

293   Ocean) using data collected from the first Arctic (November 1, 2018 to April 30, 2019) and

294   austral (May 1, 2019 to September 30, 2019) winters.

295   **4. Results**

296   **4.1 Comparisons with Sentinel-2 imagery**

297   The S-2/ATL07 comparison for the ~50 km profile (P1) within the western Weddell Sea

298   on March 17th, 2019 for strong beam 1 (*gt1l* in this backward spacecraft orientation) is shown in

299   Figure 2. This cropped S-2 image (top panel) depicts a scene of mixed ice surfaces - large

300   consolidated floes, small broken up floes, and the occasional lead opening. It also features very

301   flat/thin ice for the first ~20 km and thicker/rougher ice (relative heights ~2/2.5 m higher) for the

302   remaining 30 km along-track. The final ~5 km of the scene features clouds, as can be seen more

303   clearly in the zoomed-out Figure 1. The ATL07 radiometric surface classification scheme

304   detected 218 specular lead segments and 19 dark lead segments for this scene, with 196

305   candidate (and indeed utilized) sea surface segments. The ATL07/10 lead classification shows

306   strong agreement with the S-2 imagery. As most of the lead segments are specular, the photon

307   rate shows corresponding spikes in these same locations, along with drops in the background rate

308   (as expected from background photons scattering away from the detector over specular surfaces).

309   The scene highlights the ability of ICESat-2 to detect both narrow (10s of meters) and wide

310   (100s of meters) openings in the ice cover. Dark lead classified segments are produced at ~8 km

311   and especially at ~45-50 km along-track, with no leads visible in the imagery in both locations

312   (although in the latter it is harder to assess due to the clouds). The presence of clouds in the last

313   ~5 km corresponds with a clear attenuation in photon rate around this part of the scene, similar to

314   the Operation IceBridge comparisons given in Kwok et al., (2020c). The ~8 km along-track dark

315   lead is harder to diagnose, as this is associated with a sharp decline in photon rate, as one would

316 expect from a lead, but no obvious lead or cloud is visible in the imagery. These comparisons

317 benefit from the very small time difference (~7 minutes) between the ICESat-2 data and S-2

318 image acquisition. The derived lead fractions and chord lengths in this scene are also shown in

319 Figure 2 (panel 6). The lead fractions are estimated as 1.38% (v_1) and 1.54% (v_2), while the

320 mean chord lengths are estimated as 2.96 km (v_1) and 2.49 km (v_2). The remaining profiles using

321 the strong and weak beams are given in the Supplementary Information (Figures S1 to S5).

322 Summary statistics (lead classification counts, lead fraction and chord lengths) are provided in

323 Table 1. No obvious degradation of the classification performance is visible in the weak beam

324 profiles, although ICESat-2 generally detects fewer leads and lower lead fractions than with the

325 strong beams.

326   The S-2/ATL07 comparison for the northernmost ~50 km profile (P2) within the Lincoln

327 Sea, Arctic Ocean on May 25th, 2019 for the middle strong beam (*gt2l* in this backward

328 spacecraft orientation) is shown in Figure 3. The S-2 image depicts a scene of large consolidated

329 floes, small broken up floes/leads, but also two much larger (> 1 km) lead openings. No clouds

330 are visible in the imagery (or implied by attenuations in the photon rate). The heights extend

331 from just over 0 m to ~2-2.5 m. The ATL07 radiometric surface classification scheme detected

332 416 specular leads and 2 dark leads for this scene, with 220 candidate (and again utilized) sea

333 surface segments. The ATL07/10 lead classification again shows strong agreement with the S-2

334 imagery. It is encouraging to note that the refrozen lead of low height/freeboard at ~10 km

335 along-track is not classified as a specular or dark lead. Only a slight decline photon rate is

336 observed here. At ~15-20 km along-track, the S-2 scene shows some small but highly

337 consolidated ice floes, with some leads detected, highlighting the challenge of lead/floe detection

338 in the more consolidated ice regimes. The lead fractions for this scene are estimated as 2.55%

339 (v_1) and 6.37% (v_2), while the chord lengths are estimated as 1.82 km (v_1) and 1.99 km (v_2). The

340 difference between the v_1 and v_2 estimates are higher, and we can see this is mainly driven by the

341 inclusion (or absence) of the segments within the large lead openings. Including the extra sea

342 surface segments by using a higher (20%) height threshold in v_2 increases lead fractions, as

343 expected, however also results in the perhaps more counter intuitive result of increasing the

344 mean chord length as the ice floe groupings remain too small to be classified as a floe and are

345 simply discarded. The profiles of this image for the remaining strong and weak beams are given

346 in the Supplementary Information (Figures S6 to S10) and summarized in Table 1. We also

347   include in the Supplementary Information the profiles from P3 (Figures S11 to S16). We did not

348   include these in the main manuscript as they generally featured fewer leads compared to the P2

349   comparisons. These additional beam comparisons show again a remarkably high level of

350   agreement with the S-2 imagery in terms of the lead classification but some potentially missing

351   lead classifications within narrower cracks/leads suggested by the S-2 image. The summary

352   statistics are included in Table 1. Also noteworthy is that while the S-2 image in Figure 1 shows

353   clouds around the northwestern section of P3, no indication of clouds can be seen in the ICESat-

354   2 data (no photon rate attenuation), which is likely due to the higher time difference between the

355   ICESat-2 data and S-2 image acquisition here (~94 minutes).

356   In Figure 4 we zoom in further on the P2 profile to highlight the ICESat-2 performance

357   across this second large lead opening (at ~41 - 43 km along-track in Figure 3). The S-2 image,

358   despite being coarse when looking at this scale, suggests the presence of young gray ice within

359   this lead which is categorized as a dark lead in 2 of the ATL07 segments (note the drops in

360   photon rate compared to the increase in photon rate in the specular lead classifications). This

361   appears to be an accurate classification (they are of similar height to the surrounding specular

362   leads, so could be used to derive the reference sea surface) and highlights the potential utility of

363   the dark lead classification in ATL07/10. Another thing of note here is that due to the strict local

364   height filter in the ATL07 algorithm (Step 4 in Section 2.1) a significant fraction of these

365   segments are not classified as *candidate lead* segments (*ssh_flag* = 1). This results in some

366   erroneous ice segments and small 'chords' being included within the lead, biasing our statistics.

367   These erroneous chords are removed when we move to the higher height percentile filter (v_2),

368   resulting in an increase in chord length (0.74 km to 0.91 km) and a doubling in the lead fraction

369   (9.12% to 19.17%), albeit in this highly localized, lead profile.

370   **4.2 Basin scale assessments**

371   To better understand the sea ice classification and to provide context for the basin-scale

372   lead fraction/chord length estimates shown next, we first show basin-scale maps of key lead

373   classification metrics from ATL07 across the Arctic and Southern Ocean for the winter study

374   periods (Arctic: November 1, 2018 to April 30, 2019; Southern Ocean: May 1 2019 to

375   September 30, 2019). Figure 5 shows the radiometric lead fraction compared to all (segment

376   length weighted) segments, the ratio of radiometric specular lead segments to dark lead

377   segments, the fraction of specular lead segments that become sea surface segments (*ssh_flag* ≥ 1)

378   and the fraction of sea surface (lead) segments compared to all segments – i.e. the lead fraction.

379   The radiometric lead and sea surface lead segments generally follow the spatial pattern expected

380   from our past knowledge of the sea ice state, increases in leads (declines in concentration)

381   towards the ice edge. In both hemispheres dark leads make up a significant (~50%) fraction of

382   the total number of radiometric leads. In both hemispheres a significant (>70%) fraction of the

383   specular leads pass the height filter and are assigned as sea surface segments. There is a clear

384   increase in the fraction of discarded specular leads along the ice edge in both hemispheres, but

385   also within the Canadian Arctic Archipelago. As ATL10 applies a stricter 50% concentration

386   filter from passive microwave data to avoid wave contamination (ATL07 uses 15%), and a 25

387   km coastal mask, many of these regions adjacent to the ice edge (in both hemispheres) and near

388   coastlines will not be processed into freeboard. Sea ice concentrations from the monthly (final

389   and near-real time) NSIDC Climate Data Record (CDR, Meier et al., 2017; Meier et al., 2017)

390   averaged over this same time period across both hemispheres are given in Figure 6 for context.

391   Figure 7 shows the 25 km x 25 km gridded lead fractions calculated using the *ssh_flag*

392   ($L_f{}^{v1}$, as in Figure 5d), and also using the 20% height filter ($L_f{}^{v2}$). $L_f{}^{v2}$ consistently results in

393   higher lead fractions as expected, especially around the ice edge. We also note the increased lead

394   fractions in areas of known polynya formation - the North Water Polynya to the northwest of

395   Greenland and, to a lesser degree, Terra Nova Bay Polynya in the northern Ross Sea. Neither are

396   as visible in the passive microwave-derived concentrations (Figure 6). Mean Arctic Ocean lead

397   fraction are given as 1.06 % ($L_f{}^{v1}$) and 1.80 % ($L_f{}^{v2}$). Mean Southern Ocean lead fractions are

398   given as 0.66% ($L_f{}^{v1}$) and 1.24% ($L_f{}^{v2}$). The Southern Ocean lead fractions, while lower on

399   average, show increased lead fractions within the pack ice (compare with sea ice concentration in

400   Figure 6), especially in the eastern Southern Ocean. This is expected considering the open ocean

401   boundaries and the general divergent (away from the coast) Antarctic ice drifts. The results also

402   highlight the sensitivity of these estimates to this one aspect of the ATL07 lead finding

403   algorithm. Lead fractions within the pack ice of the Central Arctic are very low (< 1%) which we

404   discus more in the discussion/summary section.

405   Figure 8 shows the 25 km gridded chord lengths calculated using the *ssh_flag* ($C_l{}^{v1}$) and

406   the 20% height filter ($C_l{}^{v2}$). Mean Arctic Ocean chord lengths are given as 5.56 km ($C_l{}^{v1}$) and

407   5.23 km ($C_l{}^{v1}$). Mean Southern Ocean chord lengths are given as 5.43 km ($C_l{}^{v1}$) and 4.55 km

408   ($C_l{}^{v2}$). As in the lead fractions, there is high spatial variability not captured by these simple

409   hemispheric means. Lower chord lengths are produced within the eastern Arctic Ocean

410   (compared to the western Arctic Ocean) and also in the eastern Southern Ocean (compared to the

411   western Southern Ocean). The spatial variability is generally higher than the lead fraction as only

412   small changes in lead fraction can have a large impact on the derived chord lengths. The Arctic

413   shows a sharp increasing gradient within the more central Arctic region. Chord lengths are high

414   (consistently greater than 10 km) in the central Arctic, which we discuss more in the following

415   section.

416   Figure 9 shows the probability distribution of the individual chord lengths for the Arctic

417   and Southern Ocean using the $C_l{}^{v1}$ and $C_l{}^{v2}$ chord length estimates. The data are plotted on a

418   log-log scale to highlight the power law nature of the underlying distributions. The consistency

419   of the distributions across hemispheres and lead finding algorithm (*v1* and *v2*) is encouraging.

420   The distributions become more variable at the tail of the distribution (> 10 km) due to the lower

421   sampling rate of these higher chord lengths. While log-log distributions can help visually

422   highlight power-law like behavior in empirical data, more robust statistical tests are needed to

423   truly test for whether data is well characterized by a power-law, especially due to the issues with

424   the less well-observed tails of the distribution (Clauset et al., 2009; Stern et al., 2018, Horvat et

425   al., 2019). We plan to explore this in future work as we compare against the chord length

426   estimates from other observed data, as discussed below.

427   **5.   Discussion and summary**

428   The coincident Sentinel-2 (S-2)/ICESat-2 scenes provide crucial validation of the

429   ICESat-2 sea ice classification procedure, with the caveat that these represent only a small

430   fraction of the available sea ice data produced from ICESat-2 to-date. The specular lead

431   classification in the sea ice products shows strong agreement with the imagery across all beams,

432   while the reliability of the smaller quantity of dark leads found in these profiles was more

433   questionable. The Southern Ocean profile provided further evidence to that presented in Kwok et

434   al., (2020c) of their more uncertain reliability in the presence of clouds. Although the Arctic

435   Ocean profile showed 2 dark leads that appeared to be accurately classified (young, dark gray ice

436   in the imagery). More coincident S-2 scenes across different sea ice regimes (time and space)

437 would help provide further insight into the potential utility of the dark leads, especially as they

438 make up a significant fraction (~50-60%) of the total number of radiometric leads detected by the

439 current ATL07 algorithm. As discussed in Kwok et al., (2020c), the exclusion of dark leads from

440 the freeboard calculation has the downside of reducing coverage, especially in some of the more

441 consolidated sea ice regimes, providing motivation for continued study to ensure that this

442 exclusion is not overly restrictive.

443 It is interesting to note that the ATL07 segments over the relatively wide (> 1 km) leads

444 in our Arctic Ocean S-2 profile (Figure 3) are generally classified as specular, except for the 2

445 dark lead segments over regions of young, dark grey ice. Intuitively we might expect this all to

446 be considered a 'dark lead' as the larger opening increases fetch and the potential for surface

447 roughening. However, ICESat-2 segments are classified mainly as specular, until the photon rate

448 drops drastically (to less than that over the snow-covered ice) over the small region of young

449 gray ice. Similarly, the very thin cracks shown in the imagery (on the order of meters to tens of

450 meters, i.e. the segment resolution of the ATL07 data) were often classified as ice. It is unclear

451 from the S-2 imagery (10 m resolution) the extent to which these leads/cracks have refrozen and

452 thus how confident we can be in prescribing these segments as misclassified. Higher resolution

453 imagery (e.g. from Digital Globe's Worldview imagery) could provide useful further insight here

454 and will be explored in future work.

455 The local height filter included in the lead (sea surface) finding algorithm further limits

456 the number of leads identified. This appears reasonable when the goal is accurately determining

457 a reference sea level for freeboard but less ideal for deriving sea ice state information, e.g. lead

458 fraction and chord length. This study presented a crude approach to relax this height filter

459 (increasing the percentile threshold from 2% to 20%), which is worthy of further investigation as

460 we seek to increase the utility of the ICESat-2 sea ice data.

461 Validation, or at least comparisons, of our basin-scale ICESat-2 estimates of lead fraction

462 and chord length with existing observational estimates are still needed. Basin-scale lead fraction

463 estimates have been produced from various satellite sensors, e.g. NASA's Moderate Resolution

464 Imaging Spectroradiometer (MODIS) (Hoffman et al., 2019; Willmes & Heinemann, 2016) and

465 Advanced Microwave Scanning Radiometer (AMSR-E) (Röhrs & Kaleschke, 2012), and also

466 ESA'S CryoSat-2 and Envisat radar altimeters (Röhrs & Kaleschke, 2012; Tilling et al., 2019).

467   Chord length distributions have also been produced from a compilation of more sporadic

468   satellite/airborne imagery estimates (Stern et al., 2018). However, comparisons with these data

469   are hindered by the considerable differences in spatial/temporal sampling, and also the different

470   interpretations and definitions of leads across sensors and algorithms. As discussed earlier, the

471   lead classification algorithm in ATL07 appears to require clear sections of open water to trigger

472   a specular lead classification. Therefore, newly refrozen leads, which may be defined as leads in

473   other (generally coarser resolution) products, may be simply classified as ice. The radar

474   altimeter-derived estimates of lead fraction and chord length from CryoSat-2 (Tilling et al., 2019,

475   Horvat et al., 2019) provide arguably the most similar dataset for comparison/assessment. The

476   CryoSat-2 lead fractions and chord lengths shown in Tilling et al., (2019) appear consistently

477   higher and lower, respectively, than the ICESat-2 results presented here. For example, Tilling et

478   al., (2019, Figure 1) shows the percentage of CryoSat-2 waveforms classified as lead (a quantity

479   related to, but not the same as lead fraction) as ~10 % in the Central Arctic but up to ~60 % in

480   the more peripheral seas, while the chord lengths (Tilling et al., 2019, Figure 2) are ~3 km in the

481   Central Arctic and ~1 km in the peripheral seas. In contrast, the chord lengths presented in this

482   study are consistently > 10 km within the Central Arctic. There is better agreement on the

483   general spatial pattern of increasing lead fractions/decreasing chord lengths in the peripheral

484   seas, however. Radar altimeters such as CryoSat-2 are highly sensitive to the presence of

485   specular leads within the radar swath and have the added benefit of being largely unaffected by

486   clouds. However, the CryoSat-2 footprint is much larger (a pulse limited footprint of ~400 m

487   along track x 1.65 km across track, however off-nadir leads can still dominate returns from

488   within the larger beam-limited across track footprint of 15 km) than ICESat-2 (mean of ~26 m x

489   11 m for a given ATL07 strong beam segment). Future work will aim to better assess, and

490   hopefully reconcile, the lead fraction and chord length estimates from these two missions, taking

491   these significant sampling differences into account. We also hope to explore further statistical

492   testing of the power-law hypothesis for the floe length distribution, which was recently

493   challenged in Horvat et al., (2019) using CryoSat-2 chord length estimates. This reconciliation is

494   further motivated by the need to provide reliable observational constraints on the floe size

495   distributions being incorporated into sea ice components of Global Climate Models (Horvat, et

496   al., 2019). Airborne data from NASA's Operation IceBridge campaigns, which combine high-

497   resolution imagery and laser altimetry, should prove invaluable.

498   Our hope is that ICESat-2 sea ice data can be used to provide routine, and reliable, basin-
499   scale measurements of lead fraction, ice concentration and chord length estimates, in addition to
500   its primary mission requirement of delivering accurate estimates of sea ice height and freeboard.
501   Additional ICESat-2 sea ice algorithm testing and development is needed to further improve the
502   classification accuracy, which can be guided by additional comparisons with imagery (satellite
503   and airborne) and other airborne and satellite datasets. The ICESat-2 lead classification
504   algorithm utilizes fixed empirical thresholds (discussed in Section 2.1) which can easily be
505   tuned/calibrated as needed, as can other elements of the algorithm including the height percentile
506   threshold (which we simply explored in this study) and the photon aggregations. These
507   thresholds also need to be better explored in terms of appropriate strong/weak beam differences.
508   Efforts are also ongoing to provide further insight into the dark leads and their potential
509   reintroduction by utilizing a new cloud filter in the sea ice algorithm (Kwok et al., 2020c).
510   However, this assumes that the dark lead classifications unaffected by clouds are more reliable,
511   which is still unclear. The results and discussion presented here also raise the issue of how best
512   to classify newly refrozen leads or gray ice in the sea ice products, or even where exactly to draw
513   the line between sea ice and open water – another key consideration as we seek to increase the
514   utility of the ICESat-2 sea ice products.

520   **Data availability**

521   Sentinel-2 imagery was derived from Copernicus data obtained at
522   https://schihub.copernicus.eu. The ICESat-2 ATL07 (sea ice height and type) and ATL10
523   (freeboard) data products used here are available through the NSIDC (https://nsidc.org/data/atl07
524   & https://nsidc.org/data/atl10). The gridded lead fraction and chord length estimates derived in
525   this study are available on Zenodo: https://doi.org/10.5281/zenodo.4075390.

526   **References**

527   Bateson, A. W., Feltham, D. L., Schröder, D., Hosekova, L., Ridley, J. K., & Aksenov, Y.

528   (2020). Impact of sea ice floe size distribution on seasonal fragmentation and melt of

529   Arctic sea ice. *The Cryosphere*, *14*(2), 403–428. https://doi.org/10.5194/tc-14-403-2020

530   Clauset, A., Shalizi, C. R., & Newman, M. E. J. (2009). Power-law distributions in empirical

531   data. *SIAM Review*, *51*(4), 661–703. https://doi.org/10.1137/070710111

532   Feltham, D. L. (2005). Granular flow in the marginal ice zone. *Philosophical Transactions of the*

533   *Royal Society A: Mathematical, Physical and Engineering Sciences*, *363*(1832), 1677–

534   1700. https://doi.org/10.1098/rsta.2005.1601

535   Hoffman, J. P., Ackerman, S. A., Liu, Y., & Key, J. R. (2019). The Detection and

536   Characterization of Arctic Sea Ice Leads with Satellite Imagers. *Remote Sensing*, *11*(5),

537   521. https://doi.org/10.3390/rs11050521

538   Horvat, C, Roach, L. A., Tilling, R., Bitz, C. M., Fox-Kemper, B., Guider, C., et al. (2019).

539   Estimating the sea ice floe size distribution using satellite altimetry: theory, climatology,

540   and model comparison. *The Cryosphere*, *13*(11), 2869–2885. https://doi.org/10.5194/tc-

541   13-2869-2019

542   Horvat, C., Blanchard-Wrigglesworth, E., & Petty, A. (2020). Observing Waves in Sea Ice With

543   ICESat-2. *Geophysical Research Letters*, *47*(10), e2020GL087629.

544   https://doi.org/10.1029/2020GL087629

545   Horvat, C., Tziperman, E., & Campin, J.-M. (2016). Interaction of sea ice floe size, ocean eddies,

546   and sea ice melting. *Geophysical Research Letters*, *43*(15), 8083–8090.

547   https://doi.org/10.1002/2016GL069742

548   Kwok, R., Cunningham, G. F., Hoffmann, J., & Markus, T. (2016). Testing the ice-water

549   discrimination and freeboard retrieval algorithms for the ICESat-2 mission. *Remote*

550   *Sensing of Environment*, *183*, 13–25. https://doi.org/10.1016/j.rse.2016.05.011

551   Kwok, R., Petty, A. A., Cunningham, G., Hancock, D., Ivanoff, A., Wimert, J., Bagnardi, M.,

552   Kurtz, N., (2020a). Ice, Cloud, and Land Elevation Satellite-2 Project: Algorithm

553   Theoretical Basis Document (ATBD) for Sea Ice Products (ATL07/ATL10) Release

554   003,. https://doi.org/10.5067/UAZPI91070H4.

555   Kwok, R., Kacimi, S., Markus, T., Kurtz, N. T., Studinger, M., Sonntag, J. G., et al. (2019b).

556   ICESat-2 surface height and sea-ice freeboard assessed with ATM lidar acquisitions from

557   Operation IceBridge. *Geophysical Research Letters*, *44*, 11228– 11236.

558   https://doi.org/10.1029/2019GL084976

559   Kwok, R., Markus, T., Kurtz, N. T., Petty, A. A., Neumann, T. A., Farrell, S. L., et al. (2019a).

560   Surface Height and Sea Ice Freeboard of the Arctic Ocean From ICESat-2:

561   Characteristics and Early Results. *Journal of Geophysical Research: Oceans*, *124*(10),

562   6942–6959. https://doi.org/10.1029/2019JC015486

563   Kwok, R., Kacimi, S., Webster, M. A., Kurtz, N. T., & Petty, A. A. (2020b). Arctic Snow Depth

564   and Sea Ice Thickness From ICESat-2 and CryoSat-2 Freeboards: A First Examination.

565   *Journal of Geophysical Research: Oceans*, *125*(3), e2019JC016008.

566   https://doi.org/10.1029/2019JC016008

567   Kwok, R., Petty, A. A., Bagnardi, M., Kurtz, N. T., Cunningham, G. F., & Ivanoff, A. (2020c).

568   Refining the sea surface identification approach for determining freeboards in the

569   ICESat-2 sea ice products. *The Cryosphere Discussions*, 1–18. https://doi.org/10.5194/tc-

570   2020-174

571   Li, X., Krueger, S. K., Strong, C., Mace, G. G., & Benson, S. (2020). Midwinter Arctic leads

572   form and dissipate low clouds. *Nature Communications*, *11*(1), 206.

573   https://doi.org/10.1038/s41467-019-14074-5

574   Magruder, L. A., Brunt, K. M., Alonzo, M. Early ICESat-2 on-orbit Geolocation Validation

575   Using Ground-Based Corner Cube Retro-Reflectors. *Remote Sens.* 2020, *12*, 3653.

576   https://doi.org/10.3390/rs12213653

577   Markus, T., Neumann, T., Martino, A., Abdalati, W., Brunt, K., Csatho, B., et al. (2017). The

578   Ice, Cloud, and land Elevation Satellite-2 (ICESat-2): Science requirements, concept, and

579   implementation. *Remote Sensing of Environment*, *190*, 260–273.

580   https://doi.org/10.1016/j.rse.2016.12.029

581   McGill, M., Markus, T., Scott, V. S., & Neumann, T. (2013). The Multiple Altimeter Beam

582   Experimental Lidar (MABEL): An Airborne Simulator for the ICESat-2 Mission. *Journal*

583   *of Atmospheric and Oceanic Technology*, *30*(2), 345–352.

584   https://doi.org/10.1175/JTECH-D-12-00076.1

585   Meier, W. N., Fetterer, F., & Windnagel, A. K. (2017). Near-Real-Time NOAA/NSIDC Climate

586   Data Record of Passive Microwave Sea Ice Concentration, Version 1.

587   https://doi.org/10.7265/N5FF3QJ6

588   Meier, W. N., Fetterer, F., Savoie, M., Mallory, S., Duerr, R., & Stroeve, J. (2017).

589   NOAA/NSIDC Climate Data Record of Passive Microwave Sea Ice Concentration,

590   Version 3. https://doi.org/10.7265/N59P2ZTG

591   Neumann, T. A., Martino, A. J., Markus, T., Bae, S., Bock, M. R., Brenner, A. C., et al. (2019).

592   The Ice, Cloud, and Land Elevation Satellite – 2 mission: A global geolocated photon

593   product derived from the Advanced Topographic Laser Altimeter System. *Remote*

594   *Sensing of Environment*, *233*, 111325. https://doi.org/10.1016/j.rse.2019.111325

595   Petty, A. A., Kurtz, N. T., Kwok, R., Markus, T., & Neumann, T. A. (2020). Winter Arctic Sea

596   Ice Thickness From ICESat-2 Freeboards. *Journal of Geophysical Research: Oceans*,

597   *125*(5), e2019JC015764. https://doi.org/10.1029/2019JC015764

598   Roach, L. A., Horvat, C., Dean, S. M., & Bitz, C. M. (2018). An Emergent Sea Ice Floe Size

599   Distribution in a Global Coupled Ocean-Sea Ice Model. *Journal of Geophysical*

600   *Research: Oceans*, *123*(6), 4322–4337. https://doi.org/10.1029/2017JC013692

601   Röhrs, J., & Kaleschke, L. (2012). An algorithm to detect sea ice leads by using AMSR-E

602   passive microwave imagery. *The Cryosphere*, *6*(2), 343–352. https://doi.org/10.5194/tc-

603   6-343-2012

604   Rothrock, D. A., & Thorndike, A. S. (1984). Measuring the sea ice floe size distribution. *Journal*

605   *of Geophysical Research: Oceans*, *89*(C4), 6477–6486.

606   https://doi.org/10.1029/JC089iC04p06477

607   Stern, H. L., Schweiger, A. J., Zhang, J., & Steele, M. (2018). On reconciling disparate studies of

608   the sea-ice floe size distribution. *Elem Sci Anth*, *6*(1), 49.

609   https://doi.org/10.1525/elementa.304

610   Studinger, M. (2014). IceBridge Narrow Swath ATM L1B Elevation and Return Strength,

611   Version 2. *Boulder, Colorado USA. NSIDC: National Snow and Ice Data Center*.

612   https://doi.org/10.5067/CXEQS8KVIXEI.

613   Tilling, R., Ridout, A., & Shepherd, A. (2019). Assessing the Impact of Lead and Floe Sampling

614   on Arctic Sea Ice Thickness Estimates from Envisat and CryoSat-2. *Journal of*

615   *Geophysical Research: Oceans*, *124*(11), 7473–7485.

616   https://doi.org/10.1029/2019JC015232

617   Tilling, R., N. T. Kurtz, M. Bagnardi, A. A. Petty, R. Kwok (2020), Detection of Melt Ponds on

618   Arctic Summer Sea Ice from ICESat-2. *Geophysical Research Letters*, 47,

619   e2020GL090644. https://doi.org/10.1029/2020GL090644.

620   Willmes, S., & Heinemann, G. (2016). Sea-Ice Wintertime Lead Frequencies and Regional

621   Characteristics in the Arctic, 2003–2015. *Remote Sensing*, *8*(1), 4.

622   https://doi.org/10.3390/rs8010004

623   Zwally, H. J., Schutz, B., Abdalati, W., Abshire, J., Bentley, C., Brenner, A., et al. (2002).

624   ICESat's laser measurements of polar ice, atmosphere, ocean, and land. *Journal of*

625   *Geodynamics*, *34*(3–4), 405–445. https://doi.org/10.1016/S0264-3707(02)00042-X

626

627

628

629

630

631

632

633

634

635

636   **Tables**

	ground track	specular	dark lead	ssh	L_f^{v1} (%)	L_f^{v2} (%)	C_l^{v1} (km)	C_l^{v2} (km)
P1	gt1l	218	19	196	1.38	1.54	2.96	2.49
	gt1r	92	13	91	0.66	0.67	4.51	4.51
	gt2l	387	8	328	2.58	3.14	1.52	1.37
	gt2r	293	4	185	1.53	2.40	2.12	2.20
	gt3l	181	0	151	1.26	1.55	2.63	2.63
	gt3r	258	0	128	0.91	1.76	2.49	2.47
P2	gt1l	127	8	108	0.85	1.08	4.43	4.42
	gt1r	105	5	66	0.42	0.68	4.88	4.42
	gt2l	416	2	220	2.55	6.37	1.82	1.99
	gt2r	270	0	118	0.94	2.03	2.49	3.11
	gt3l	37	0	36	0.27	0.28	4.91	4.91
	gt3r	40	0	35	0.25	0.28	7.01	7.00
P3	gt1l	13	1	13	0.13	0.13	16.0	16.0
	gt1r	11	0	11	0.07	0.07	16.0	16.0
	gt2l	89	0	74	0.84	1.04	3.95	3.95
	gt2r	70	0	24	0.19	0.53	6.80	7.88
	gt3l	12	0	12	0.09	0.09	16.0	16.0
	gt3r	17	0	17	0.12	0.12	12.0	12.0

637   **Table 1**: Summary statistics of the ICESat-2 data in the three S-2 profiles (P1 - P3 in Figure 1)
638   across all six beams. Strong beams in this orientation are shaded gray. Columns 2-4: Number of
639   specular lead segments: *height_segment_type* = 2 - 4, dark leads segments: *height_segment_type*
640   = 5 - 9, sea surface segments: *ssh_flag* = 1 or 2 (all candidate lead segments become lead
641   segments in these profiles). Note that no cloud segment classifications were found in these
642   profiles, so they were not included in the Table. Columns 5-8: Lead fraction and chord length
643   estimates using our two different (*v₁ and v₂*) metrics.

644 **Figures**
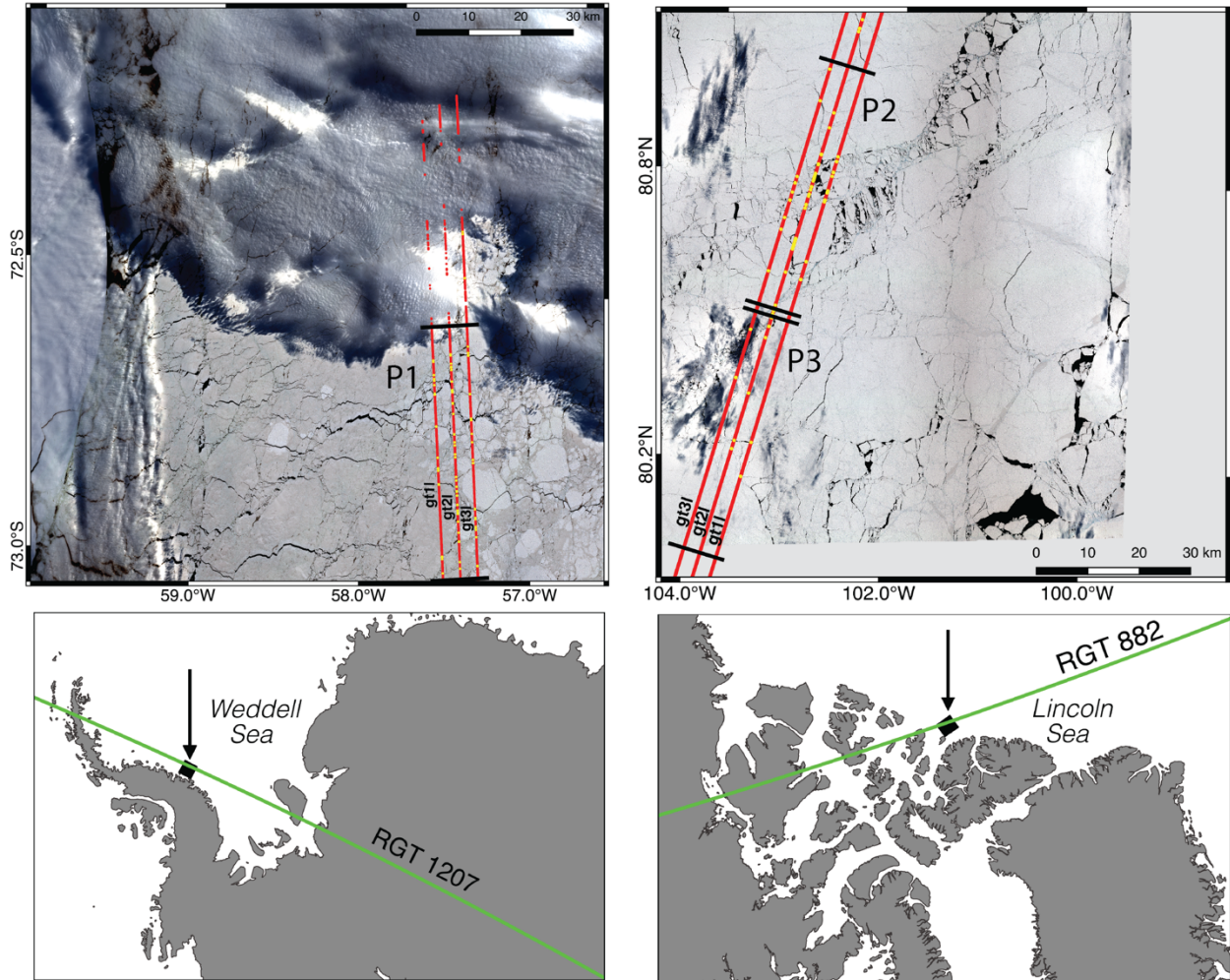
645

646 **Figure 1**: ICESat-2 ATL07 strong beam data overlaid on near-coincident Sentinel-2 RGB image
647 of (left) the Western Weddell Sea, Southern Ocean, on March 17th, 2019 and (right) the Lincoln
648 Sea of the Arctic Ocean on May 25th, 2019. The time difference between the ICESat-2 and
649 Sentinel-2 overpass for the Weddell Sea scene is ~7 minutes (ICESat-2 acquisition at 12:29
650 UTC, Sentinel-2 acquisition at 12:22 UTC), time difference for the Lincoln Sea scene is ~94
651 minutes (ICESat-2 acquisition at 00:36 UTC on 26 May 2019, Sentinel-2 acquisition at 23:01
652 UTC on 25 May 2019). Red segments are classified as sea ice (*ssh_flag* = 0), yellow segments
653 are classified as leads (*ssh_flag* ≥ 1). The ICESat-2 footprint is not to scale. P1-P3 indicate the
654 ~50 km profiles shown in Figures 2 and 3 and the Supplementary Information respectively.

655
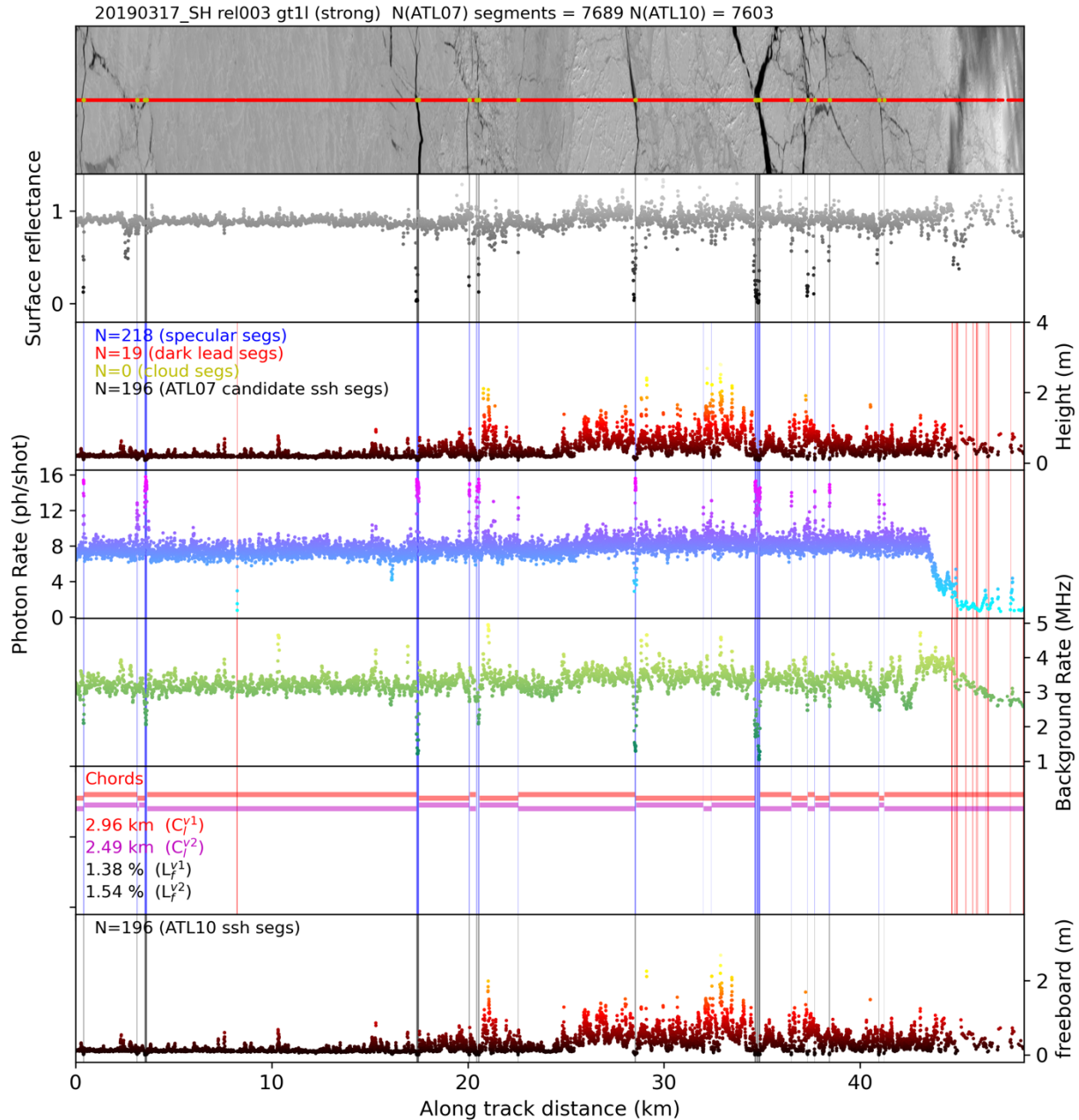
Figure 2: ICESat-2 ATL07 data from the *gt1l* ground-track (strong beam in this spacecraft orientation) overlaid on Sentinel-2 RGB imagery for a ~ 50 km profile in the Western Weddell Sea on March 17th, 2019 (P1, see Figure 1 for location). (top panel) Sentinel image with ICESat-2 profile overlaid showing the sea surface flag (*ssh_flag*, red = ice, yellow = sea surface); (second panel) surface reflectance calculated from the red band of the Sentinel-2 image from nearest neighbor pixels to the ICESat-2 profile; (panels 3-5) segment height, photon rate and background rate respectively from ATL07. Grey shading in panels 2-3 indicate *candidate* leads

664   (*ssh_flag* = 1) while in panels 4-5, blue shading indicates specular lead classifications

665   (*height_segment_type* = 2 to 5) and red shading indicates dark lead classifications

666   (*height_segment_type* = 6 to 9). Panel 7 shows the derived chord lengths as horizontal bars (red

667   = v_1, magenta = v_2) with each chord grouping shifted vertically to indicate the groups, and

668   statistics of the mean chord lengths and lead fractions using these two approaches. Panel 8 shows

669   the freeboard in ATL10, with the shading indicating actual leads used to derive reference sea

670   surface (*ssh_flag* = 2). N indicates the number of segments in ATL07 and ATL10 as specified.

671

672
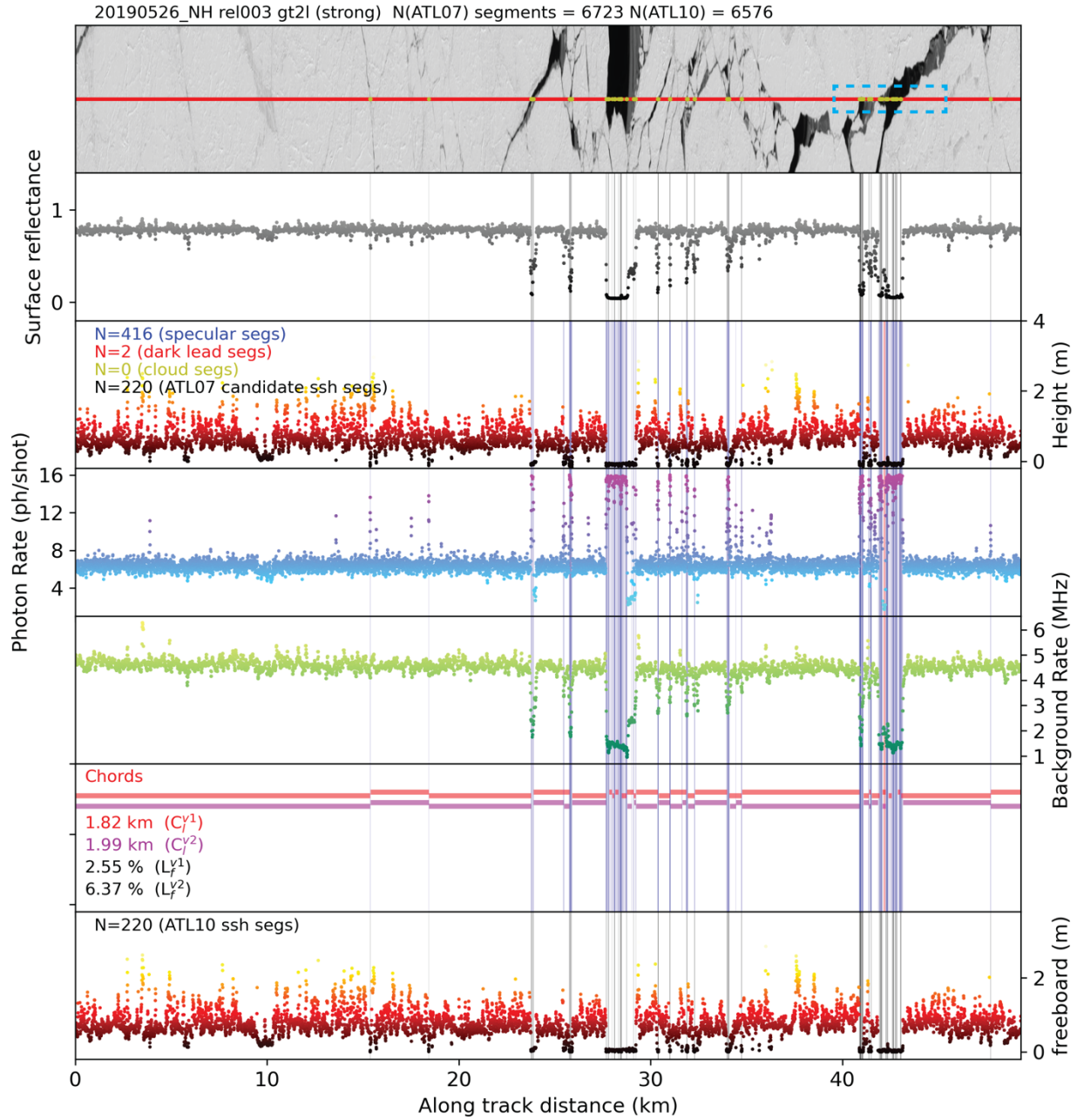
Figure 3: As in Figure 2 but for the P2 profile over the Lincoln Sea of the Arctic Ocean on May

26th, 2019 for the *gt2l* ground-track (strong beam in this spacecraft orientation) (see Figure 1 for

location). The cyan box in the top panel shows the location of the zoomed in profile in Figure 4.
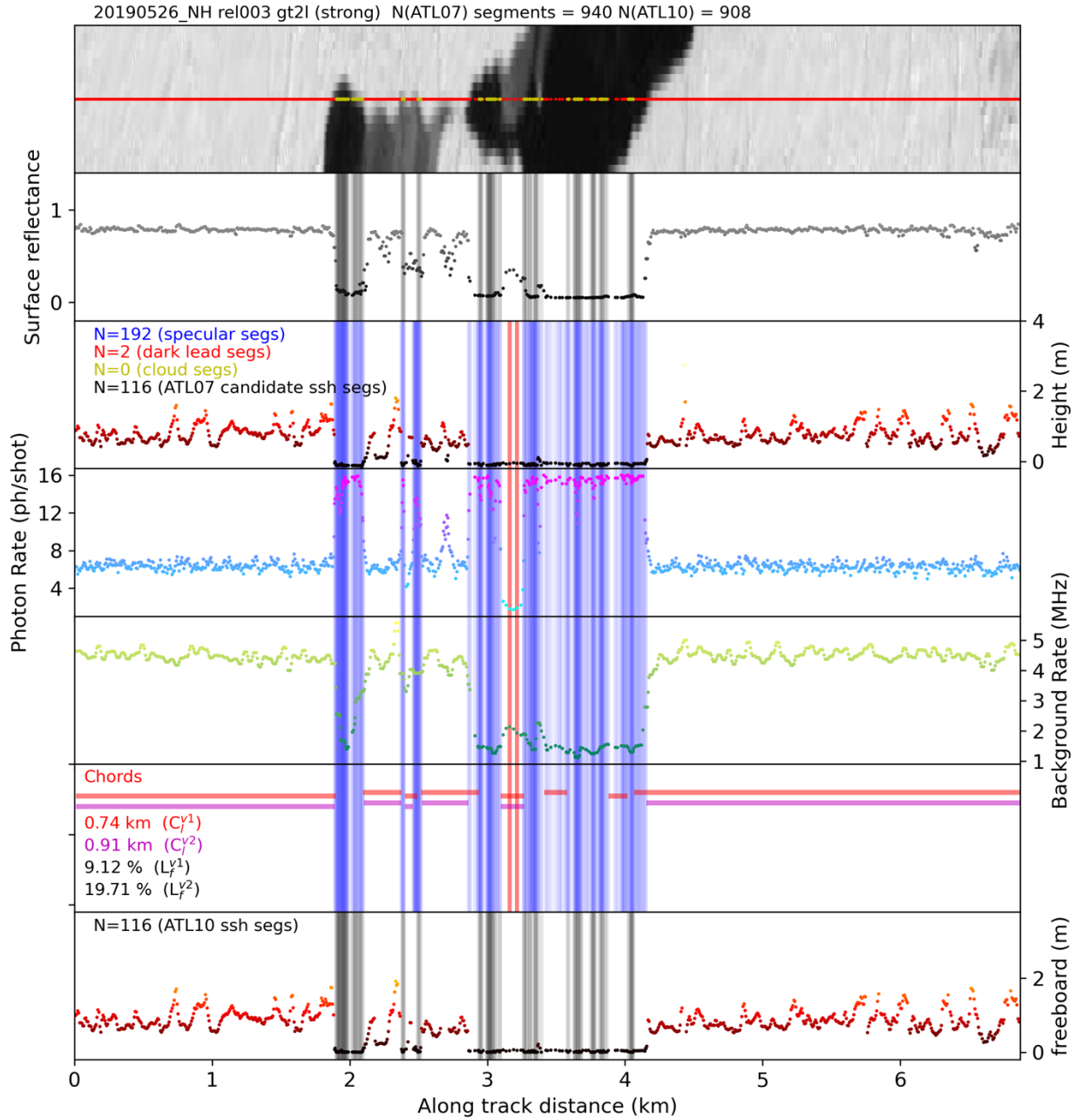
Figure 4: As in Figure 3 (P2 profile) but zoomed in on the second large lead opening (cyan box in Figure 3).
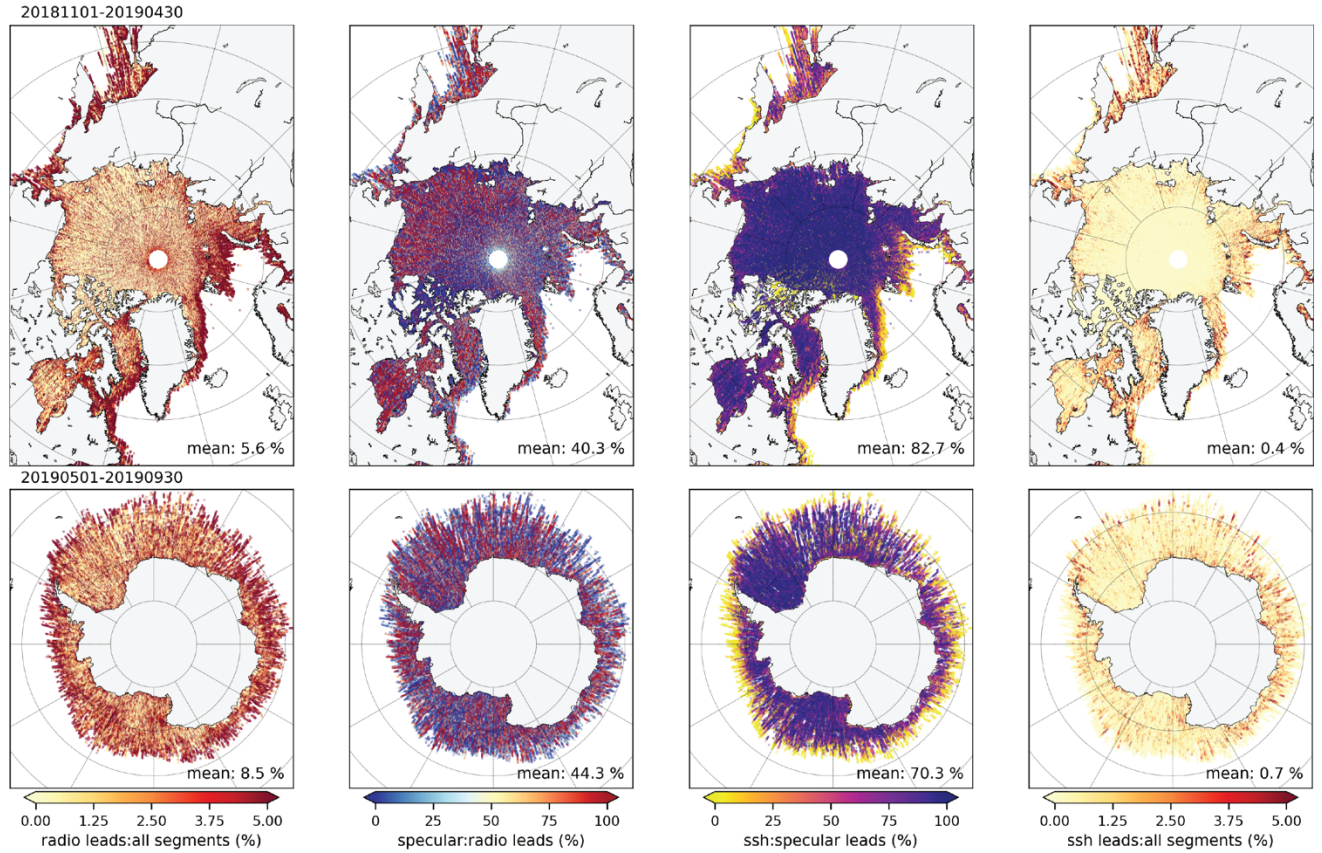
Figure 5: (first column) percent of all ATL07 segments classified as radiometric leads (*height_segment_type* = 2 to 9), (second column) percent of radiometric leads classified as specular (*height_segment_type* = 2 to 5), (third column) percent of specular leads that become sea surface segments (*ssh_flag* ≥ 1), (fourth column) percent of all height segments that become sea surface segments. (Top row) Arctic Ocean, November 1 to April 30, 2019, (bottom row) Southern Ocean, May 1 to September 30, 2019. All these percentages are calculated in 10 km along-track sections across the three strong beams and are segment length weighted.
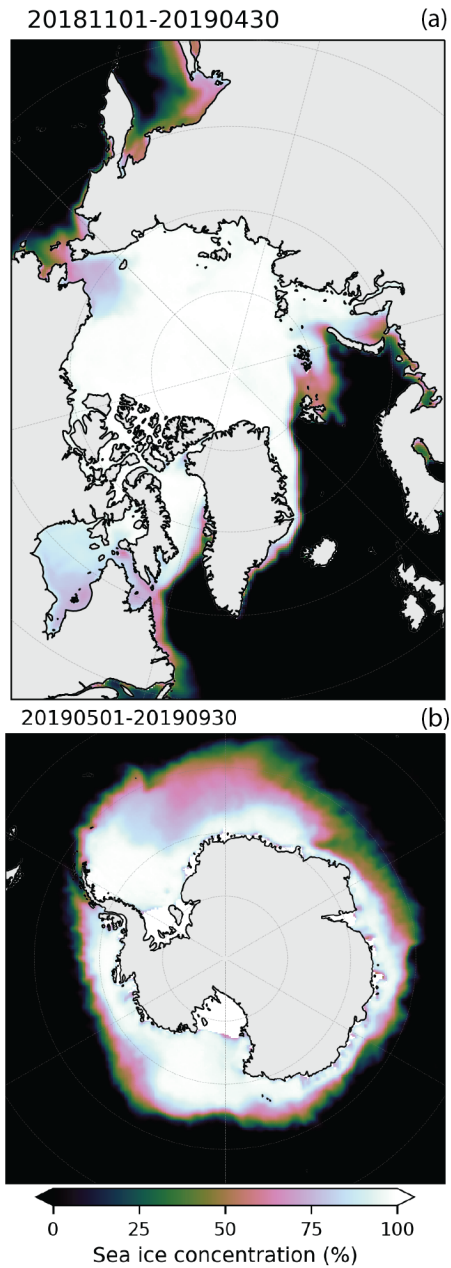
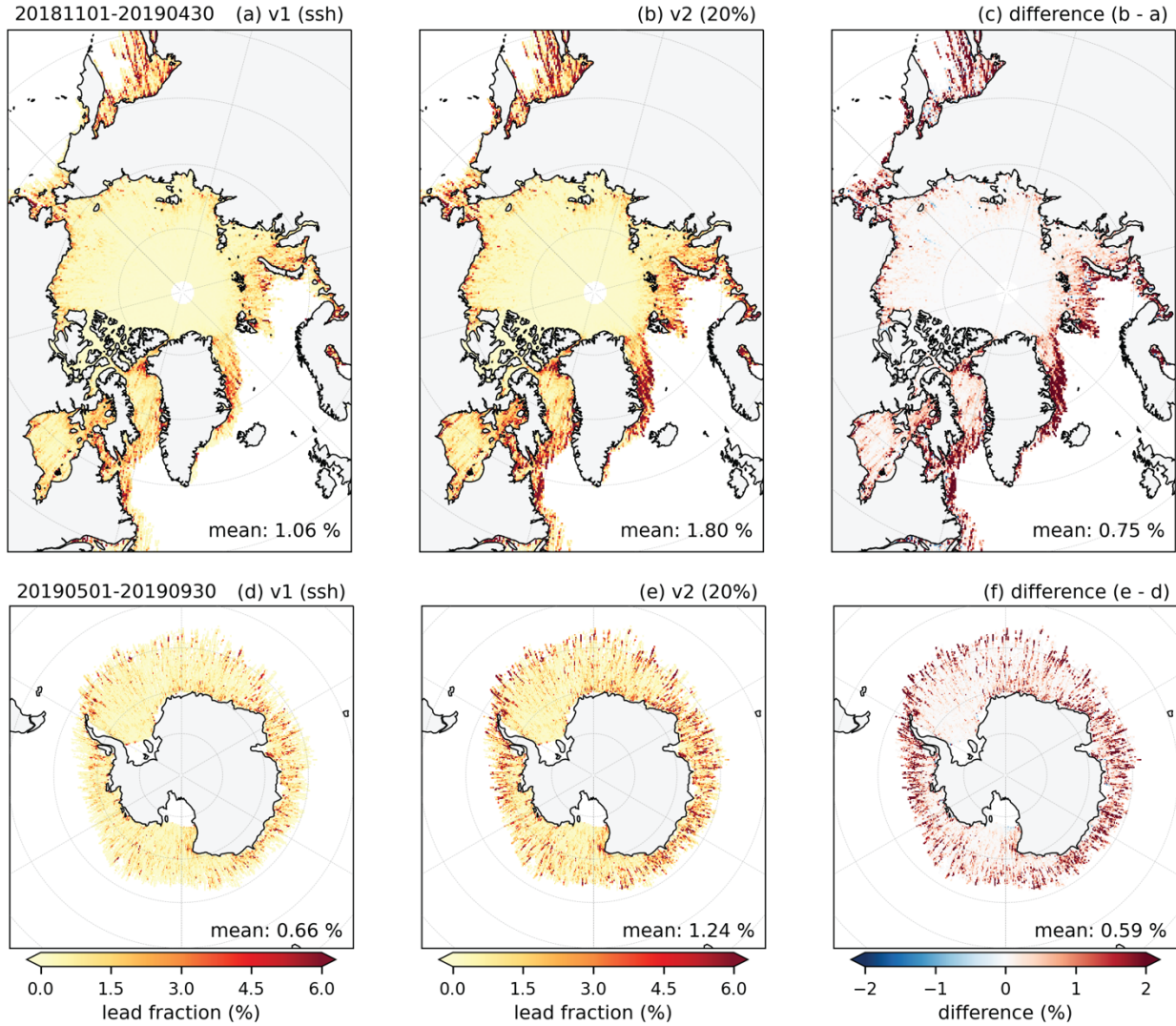**Figure 6:** Mean winter sea ice concentration derived from passive microwave data (Climate Data Record, CDR) for the (a) Arctic Ocean, November 1, 2018 to April 30, 2019 and (b) Southern Ocean, May 1 to September 30, 2019.

**Figure 7:** Lead fraction using (a and d) the *ssh_flag* (L_f^{v1}) and (b and e) the higher 20% height filter (L_f^{v2}) and the difference (c = b minus a, f = e minus d). Data are for the (top row) Arctic Ocean, November 1 to April 30, 2019, (bottom row) Southern Ocean, May 1 to September 30, 2019. All the fractions are calculated in 10 km along-track sections across the three strong beams and are segment length weighted. Data have binned to a 25 km x 25 km polar stereographic grid.

701
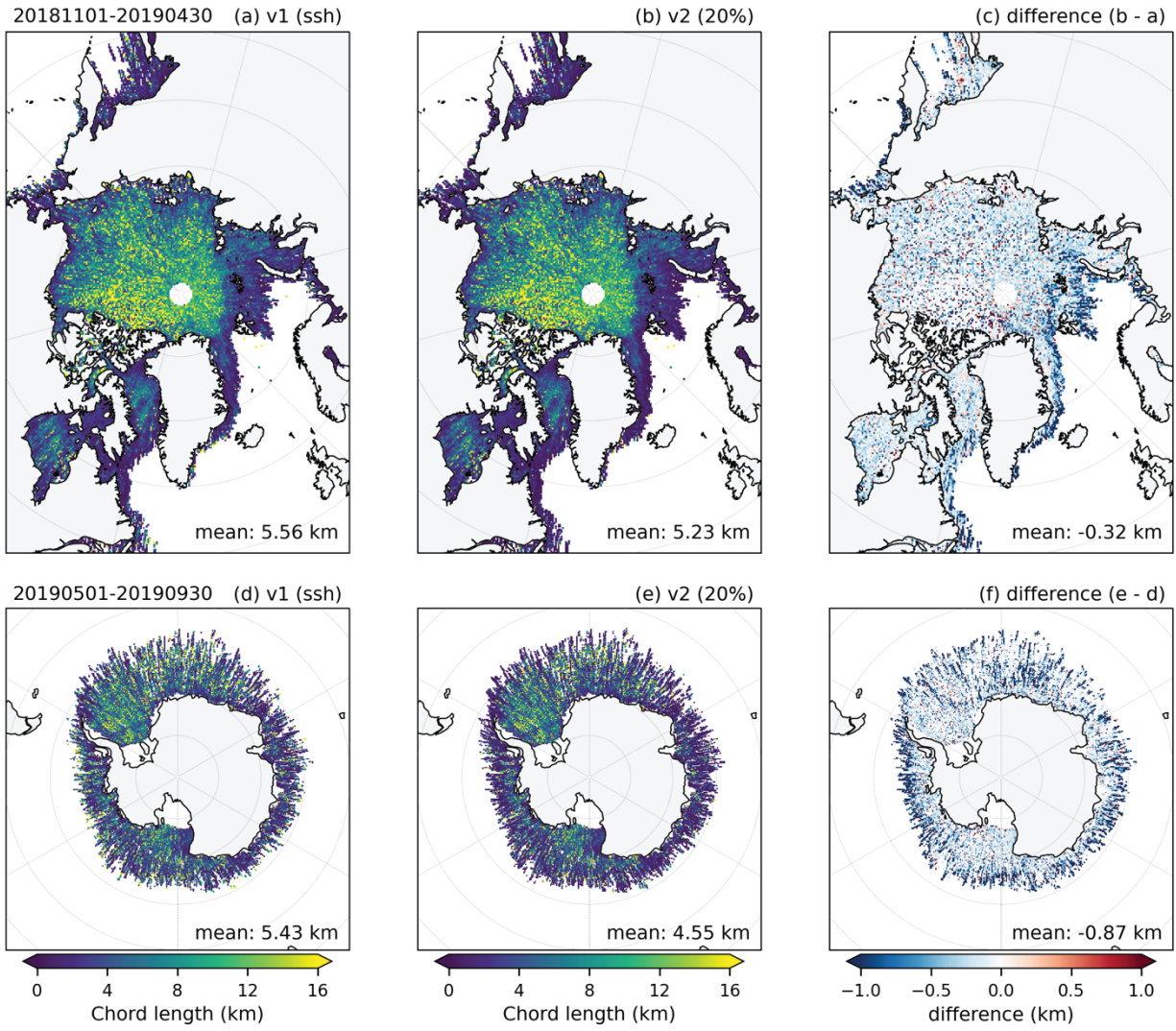
Figure 8: As in Figure 7 but for chord length (left) C_l^{v1} and (middle) C_l^{v2} and difference (right).
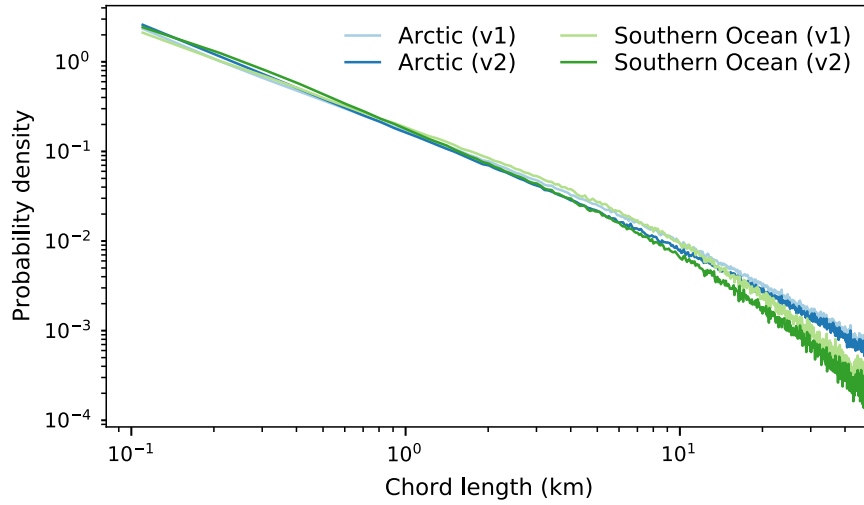
703

704   **Figure 9:** Probability distributions of the Arctic and Southern Ocean chord lengths (v1: C_l^{v1} and

705   v2: C_l^{v2}) for the same winter-time periods as in Figure 8. Distributions are plotted on a log-log

706   scale.

707